Noname manuscript No.
(will be inserted by the editor)

Filling Missing Data and Smoothing Altered Data in Satellite Imagery with a Spatial Functional Procedure

Militino, A. F. · Ugarte, M. D. · Montesino M.

Received: date / Accepted: date

Abstract Outliers and missing data are commonly found in satellite imagery. These are usually caused by atmospheric or electronic failures, hampering the correct monitoring of remote-sensing data. To avoid distorted data, we propose a procedure called "spatial functional prediction" (SFP). The SFP procedure consists of the following: 1) aggregating remote-sensing data for reducing the number of missing data and/or outliers; 2) additively decomposing the time series of images into a trend, a seasonal, and an error component; 3) defining the spatial functional data and predicting the trend component using an ordinary kriging; and 4) adding back the seasonal and error components to the predicted trend. The benefits of the SFP procedure are illustrated in the following scenarios: introducing random outliers, random missing data, mixtures of both, and artificial clouds in an extensive simulation study of composite images, and using daily images with real clouds. The following two derived variables are considered: land surface temperature (LST day) and normalized vegetation index (NDVI), which are obtained as remote-sensing data in a region in northern Spain during 2003-2016. The performance of SFP was checked using the root mean square error (RMSE). A comparison with a procedure based on predicting with thin-plate splines (TpsP) is also made. We conclude that SFP is simpler and faster than TpsP, and provides smaller values of RMSE.

Keywords Geostatistics; Remote-Sensing Data; Spatial Dependence; Thin-Plate Splines

Militino, A. F.
Department of Statistics, Computer Science and Mathematics, and InaMat, Public University of Navarre, 31006 Pamplona, Spain

Ugarte, M. D.
Department of Statistics, Computer Science and Mathematics, and InaMat, Public University of Navarre, 31006 Pamplona, Spain
Tel.: +34-948-169202
E-mail: lola@unavarra.es

Montesino, M.
Department of Statistics, Computer Science and Mathematics, and InaMat, Public University of Navarre, 31006 Pamplona, Spain.

1 Introduction

Satellite imagery provides a powerful and effective means for describing and monitoring a great variety of information related to urbanization, pollution, deforestation, climate change, sea level, and many others agricultural or environmental applications (see for example Xu et al., 2015; Van de Kassteele et al., 2006; Park et al., 2018). Long-term changes of many derived variables and vegetation indexes are now easier to analyse because of the free availability of satellite imagery. Today, there are several platforms for retrieving the time series of remote-sensing data from sensors or satellites, with simple or composite images. Specifically, Land+Satellite (LANDSAT), SENTINEL, National Oceanic and Atmospheric Administration (NOAA), and Moderate Resolution Imaging Spectroradiometer (MODIS) are among the most popular platforms, which all provide the time series of composite and raw images after a pre-processing step to make them radiometrically and spatially comparable. This requirement is necessary because climatological seasons have different radiometric conditions coming from solar angles and meteorological conditions (Richter, 1996). Geometric corrections are also recommended for ascertaining that corresponding pixels refer to the same geographic location.

Pre-processed images can still exhibit clouds or atmospheric distortions that need to be removed. Each satellite mission uses different algorithms for processing the images and providing shorter time series of the composite images. For example, NDVI images are commonly processed with the maximum value compositing (MVC) method, based on re-assigning the maximum value of NDVI to the same pixel of the composite period (Holben, 1986). The result is a smaller number of output images with regard to the original time-series set, but better optimization of data is achieved. This technique also suppresses clouds, atmospheric and radiometric effects and reduces the directional reflectance and off-nadir viewing effects. MODIS, LANDSAT and NOAA provide periodically 16-day composite NDVI and 8-day composite LST scenes. LST day composite images are obtained by averaging an 8-day composite period.

When using daily images, different alternatives have been developed for removing clouds that do not require composite images as follows: regression methods (e.g. Zhang et al., 2014; Brooks et al., 2018), smoothing methods (Cai et al., 2017), wavelet transform (Qiu et al., 2016), wavelet-based fusion method (Tseng et al., 2008), information cloning through Poisson equations (Bhavya and Jaleel, 2014), machine-learning techniques (Hou et al., 2019), homoformic filter (Shen et al., 2014), and direct sampling methods (Yin et al., 2016). Specific applications can be found in snow cover (Gao et al., 2010; Xie et al., 2009), forestry (Masek et al., 2013), land cover change (Schneider, 2012; Masek et al., 2006), or vegetation (Yang et al., 2015; Müller et al., 2015). However, among the most popular filling and smoothing methods are those based on filtering or harmonic analysis, which is popular because of its accessibility and easy execution in free available software, which is the case of Timesat (Eklundh and Jönsson, 2012) based on the following three filtering options: double logistic, asymmetric Gaussian and Savitzky Golay, and Hants (Verhoef et al., 1996) based on the harmonic analysis of time series. Both procedures are based on mathematical approximations and do not use the basic essentials of stochastic dependence.

Geostatistical techniques (Cressie and Wikle, 2015) are still scarcely used for filling gaps or smoothing process in multi-temporal remote-sensing data; however, their use in this area was claimed many years ago (Rossi et al., 1994). A novel comparison of MVC, co-kriging and kriging methods for filling clouded pixels in NOAA-AVHRR images was already made in Addink (1999), where using the images of subsequent days as covariables enabled the use of spatio-temporal information. In this case, co-kriging outperformed the other alternatives. Overall, incorporating spatio-temporal stochastic dependence increases the computational complexity when managing large amounts of data, and therefore, providing fast, simple and efficient ways of processing the time series of images is still an active research field. Recent examples are explained next. A hybrid generalised additive model and geo-statistical space-time model have been recently published by Poggio et al. (2012) for fitting a smooth spatio-temporal trend, and a state-space model that accounts for spatio-temporal dependence (Militino et al., 2017), thin-plate splines for modelling anomalies that use ground-truth data for improving the prediction quality (Militino et al., 2018), and a quantile regression method called Gapfill (Gerber et al., 2018, 2016) have also been proposed.

In this work, we focus on filling clouds, filling sparse missing data, and removing outliers in satellite imagery using an ordinary kriging model of spatial functional data (Delicado et al., 2010). The procedure is compared with an alternative prediction method based on thin-plate splines (hereafter called TpsP) that also considers spatial dependence. The accuracy of both prediction methods will be also assessed in a simulation study. Theoretically, the time series of composite NDVI images and composite LST day images are free of outliers and missing data. Hence, the time series of composite images are used as ground-truth data references in the simulation study, where random sets of missing data, altered data, and mixtures of both are introduced in different scenarios. Additionally, six daily images of remote-sensing LST day and NDVI data free of clouds are defined as a set of ground-truth data that will be masked with the real clouds of other days. We run SFP and TpsP procedures in both scenarios and compare the results with the ground-truth images through the root mean square error (RMSE). Figure 1 shows the flowchart of the two main processes followed in the paper: the simulation study over composite LST and NDVI images, and the application for removing real clouds over daily clean images masked on purpose with real clouds, for checking the prediction accuracy.

This paper is organized as follows: Section 2 describes the procedure used in this paper, and it is split into three subsections. In the first subsection, we describe the principles of the spatial functional data analysis (SFDA) procedure; in the second subsection, we introduce the proposed spatial functional procedure (SFP); and in the third subsection, we introduce the thin-plate spline prediction (TpsP) alternative. Section 3 explains how to retrieve from MODIS the LST and NDVI composite and daily images used in the paper. An extensive simulation study evaluating the performance of SFP and TpsP using a long time series of composite images is described in Section 4, while in Section 5, both procedures are compared in terms of filling daily images for the following two derived variables: LST and NDVI. Finally, Section 6 presents the conclusions.

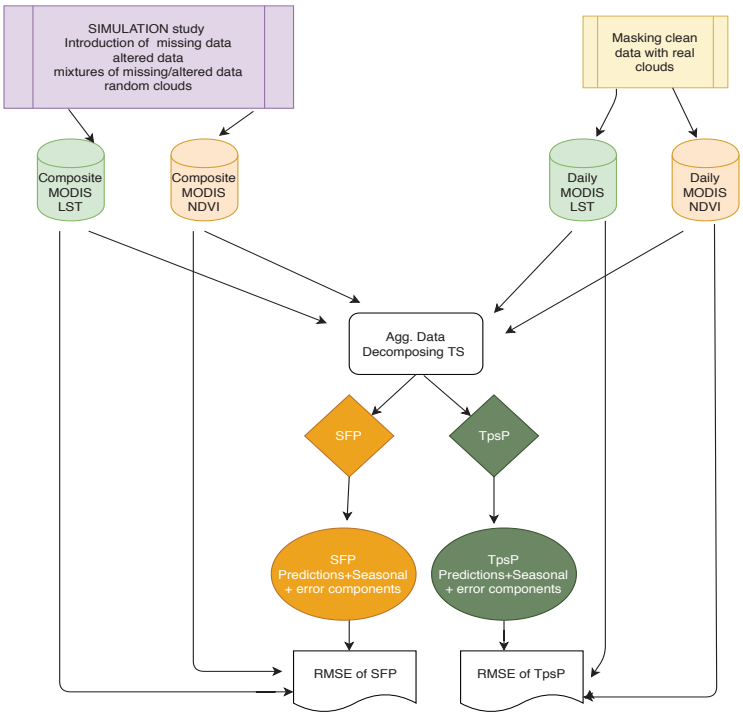

Fig. 1 Flowchart of the two main processes: the simulation study over composite LST and NDVI images and application for removing clouds in daily images. SFP and TpsP previously required aggregating data and decomposing the time series of images. Final predictions are obtained adding the seasonal and error components to the SFP and TpsP predictions. Both are checked with the root mean square error (RMSE).

2 Gap-filling and smoothing methods

2.1 Spatial Functional Data Analysis (SFDA)

Functional data analysis (FDA) is a branch of statistics that deals with analysing and modelling data in the form of random functions (Ramsay and Silverman, 2007; Vera et al., 2017; Ruiz-Medina and Espejo, 2012). Here, the functional data are defined as the time series of remote-sensing data in each pixel of a given image. The estimated model provides the prediction of the variable at unobservable locations. Predicting surfaces of geographical evolution at unobserved time points may be also achieved (Aguilera-Morillo et al., 2017).

Traditionally, the functions are obtained as independent realizations of a functional random variable, taking values in a functional space defined on a continuous domain. However, considering univariate functional data with spatial dependence is also possible. In this case, the sample dataset is given by a set of spatially corre-

lated curves, where each curve corresponds to different geographical locations on a spatial domain. Functional data are spatially correlated in a similar way as in classical geostatistics.

Specifically, an extension of the FDA to a curve kriging predictor for spatial data was done by Goulard and Voltz (1993) using a curve kriging approach and two cokriging approaches. The first approach provides predictions based on a weighted sum of scalar weights and curves. It is called ordinary kriging for function-valued data. In Giraldo et al. (2010) the authors extend this idea weighting the observed curves with functional parameters depending on t. The curves and the funcional parameters are expanded in terms of a set of basis functions. For estimating the coefficients of these basis functions, different for each functional parameter, the authors use corregionalization, and for choosing the number of basis functions they use cross-validation. This approach is called point-wise functional kriging.

Delicado et al. (2010) review the different procedures for predicting spatial functional data and compare the results obtained with the Canadian temperature data by using ordinary kriging for function-valued data, point-wise functional kriging, and functional kriging. The functional kriging approach is similar to the functional linear model for functional responses, called total model, and introduced by Ramsay and Silverman (2007). In Delicado et al. (2010) paper the authors also introduce the use of the function data theory for point processes and areal data.

Giraldo et al. (2011) propose the spatial prediction of functional data through a non-parametric fitting preprocess of data curves using B-splines (yet other alternatives are also available) using a smoothing parameter chosen by functional cross-validation. This proposal formally coincides with the functional kriging introduced by Goulard and Voltz (1993). One of the advantages of this method is that the computational cost of the procedure is similar to the classical ordinary kriging. In this work we apply the approach made with ordinary kriging for function-valued data given in Giraldo et al. (2012).

Then, a spatial functional process is defined as

$$\{\boldsymbol{Z}_s(t) : t \in T, s \in D \subseteq \Re^2\}, \tag{1}$$

where $\boldsymbol{Z}_s(t)$ are real-functional random variables depending on time t, s is the location in the Euclidean space, and D is a set in $\Re^2$. Assuming that the functional random process (1) is second-order stationary and isotropic, the curve kriging predictor is obtained as

$$\hat{\boldsymbol{Z}}_{s_0}(t) = \sum_{i=1}^{n} \lambda_i \boldsymbol{Z}_{s_i}(t), \qquad \lambda_1, \ldots, \lambda_n \in R. \tag{2}$$

Predictor (2) is an ordinary kriging predictor. It is an unbiased when $\sum \lambda_i = 1$, and it is obtained by minimising:

$$E\|\hat{\boldsymbol{Z}}_{s_0}(t) - \boldsymbol{\chi}_{s_0}(t)\|^2 = \int_T E(\hat{\boldsymbol{Z}}_{s_0}(t) - \boldsymbol{Z}_{s_0}(t))^2 dt. \tag{3}$$

The predictor has an expression similar to the classical ordinary linear predictor, but it uses curves instead of variables and becomes the best unbiased linear predic-

tor (BLUP), where each observed function can be expressed in terms of K-based functions $B_1(t), \ldots, B_K(t)$. Then,

$$z_{s_i}(t) = \sum_{j=1}^{K} a_{ij} B_j(t) = \mathbf{a}_i^t \mathbf{B}(t), \quad i = 1, \ldots, n, \tag{4}$$

where $z_{s_i}(t)$ is the observed variable (LST or NDVI) at location $s_i = (x_i, y_i)$ from $i = 1, \ldots, n$, n is the total number of pixels in the target image, $\mathbf{a}_i^t = (a_{i1}, \ldots, a_{iK})$, and $\mathbf{B} = (B_1(t), \ldots, B_K(t))$ can be Fourier or B-spline expansions, yet the B-spline functions are recommended when we do not expect any strongly cyclic variation (Ramsay, 2005).

2.2 Spatial Functional Prediction (SFP) Procedure

The spatial functional prediction (SFP) procedure is based on spatial functional data analysis (SFDA). It may be used for gap-filling processes and removing outliers in the short and long time series of satellite images. SFP consists of four steps. The first two steps prepare the input images to become spatial functional data, and the last two steps apply the ordinary kriging procedure for the spatial functional data through the `okfd` command of the `geofd` R package. The model predictions are obtained in the original image resolution of the input time series. More precisely:

1) FIRST STEP: the remote-sensing data of every input image are aggregated in windows of $x \times x$ pixels. By default, $x = 4$, though the window size can be changed, which means that we shrink the original resolution of the image by an x factor; therefore, if the input image has n pixels, after aggregation, it will have approximately $n/4$ pixels. The mean aggregation is recommended for missing data and clouds of missing data, but the median aggregation is an alternative for altered data and mixtures of missing/altered data. The appropriate factor of the aggregation depends on both the image resolution, and on the computational cost, but the results can change due to the aggregation factor. The simulation study shown in this paper recommends using factor 4 because of the trade-off between precision and computational cost. Lower factors lead to smaller reductions of missing or altered data, and higher factors may lead to over-smoothing.

This step does not guarantee the disappearance of all the missing data, but at least much missing data can be avoided. If there are still missing data, a new average process is needed. Now, every empty pixel is filled with the mean of the remote-sensing data calculated across all the image time series for the same pixel. If all of them are missing, we can fill them using the mean/median of the previous, subsequent or nearby pixels. In this process, we do not shrink the resolution of the image. We can avoid the aggregation step and the decomposition process in the original resolution of the image, but the remote-sensing data of pre-processed images can show great variability among close pixels, and therefore, the aggregation is important for the previous smoothing of the target input dataset. In addition, the aggregation step reduces the dimensionality of the problem and facilitates the optimization procedure.

2) SECOND STEP: the new time series of the aggregated and averaged input images are additively decomposed into a trend, a seasonal, and an error component,

which means that for each input time series, we derive three image time series corresponding to the three components. The decomposition step is based on a moving average procedure that loses some of the first and last images of the trend and error component of the time series. For example, in monthly time series, we lose the first six and last six images, and in daily images, we lose the first four and last four images, depending on the size of the moving average. This is a necessary step because spatial functional data analysis requires a reasonable set of smooth input functions for defining the B-spline or Fourier basis functions. Therefore, the time series of the trend component images can easily define a smooth functional dataset. Although a moving average procedure has been used in this step because it is simple and does not need specific assumptions, other procedures such as loess curves (Cleveland et al., 1990) or Kalman filtering (Durbin and Koopman, 2002) could also be used.

3) THIRD STEP: we predict the variable of interest in all the pixels of every image of the trend component using the okfd spatial functional ordinary kriging procedure in the geofd R package (Giraldo et al., 2012). This procedure defines a B-splines basis through the fda, splines, and Matrix dependence packages, and fits an ordinary kriging to the spatial functional data using geoR. Therefore, the fitted covariance functions belong to the Matérn family. Initial values of variances, nugget, and kappa coefficients are necessary to provide the starting values of the estimation procedure. The predictions are calculated in the original image resolution. Stationarity and isotropy assumptions have been empirically checked through plots of spatial functional data. See an example of the simulation study in Figure 2, where the functional data present reasonable constant means and variances.

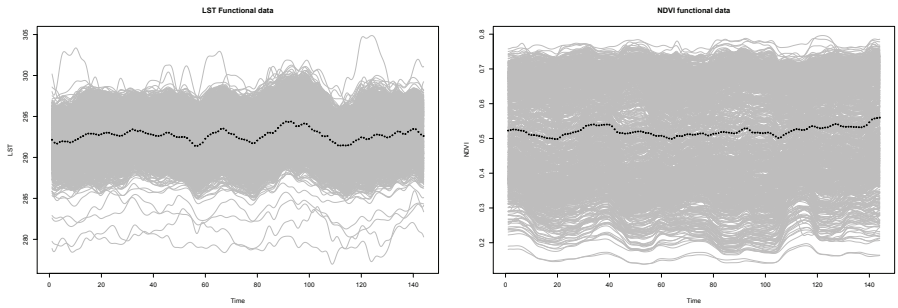

Fig. 2 LST and NDVI spatial functional data and functional mean in the simulation study

4) FOURTH STEP: we add back the seasonal and error component of the time series of images to the predicted trend. These components are added to the predictions after being projected to the original image resolution.

The quality of the predictions is checked with the root mean square error (RMSE), defined as follows:

$$RMSE(l,p) = \sqrt{\frac{\sum_{s_i,t_j}(z_{s_i t_j lp} - \hat{z}_{s_i t_j lp})^2}{IT}}, \quad (5)$$
$$s_i = 1,\ldots,I$$
$$t_j = 1,\ldots,T$$
$$l = \text{LST day, NDVI, and}$$
$$p = \{\text{SFP, TpsP}\}$$

where $z_{s_i t_j}$ and $\hat{z}_{s_i t_j}$ are, respectively, the observed and predicted values of the remote-sensing data at the locations $\mathbf{s} = (s_1,\ldots,s_m)$, I is the number of pixels of the target set, T is the number of involved images, l is the remote-sensing data, and p is the smoothing procedure.

2.3 The Thin-plate Spline Prediction (TpsP) Method

The thin-plate spline prediction (TpsP) procedure consists of applying a thin-plate spline (Tps) model to the trend component of the input times series of images, which means that TpsP repeats steps 1), 2), and 4) of the SFP procedure. However, in step 3), the TpsP predictions of the remote-sensing data are obtained separately for every image of the trend component time series. In this method, different thin-plate spline models are needed for every image.
The Tps model smooths or interpolates data (Wood, 2003, 2017), and it has been widely used in many environmental applications (e.g. Boer et al., 2001; Bernardi et al., 2017; Goitía et al., 2005). Let z_{s_i} be any derived variable observed at location $s_i = (x_i, y_i)$, from $i = 1,\ldots,n$, where n is the total number of pixels in the target image. The thin-plate spline model is expressed as

$$z_{s_i} = f(\mathbf{x}_{s_i}, \mathbf{y}_{s_i}) + \epsilon_{s_i}, \quad i = 1,\ldots,n, \quad (6)$$

where $f(\mathbf{x}_{s_i}, \mathbf{y}_{s_i})$ is an unknown deterministic smooth function, and the error vector ϵ_{s_i} is normally distributed with zero mean and variance σ^2. The second-order thin-plate spline minimizes this expression:

$$S_w = \frac{1}{n}\sum_{i=1}^{n}(z_{s_i} - f(x_i,y_i))^2 + w\int_{-\infty}^{\infty}\int_{-\infty}^{\infty}\left[\left(\frac{\partial^2 f}{\partial x^2}\right)^2 + \left(\frac{\partial^2 f}{\partial y^2}\right)^2 + 2\left(\frac{\partial^2 f}{\partial x^2 y^2}\right)^2\right]dxdy, \quad (7)$$

which corresponds to the residual sum of squares plus a constraint, depending on the smoothness level. In Equation (7), the Lagrange multiplier w controls the degree of smoothing. When $w = 0$ data are interpolated and when $w = \infty$, a polynomial is fitted (Wood, 2003). The minimization problem is solved by

$$\hat{f}(\mathbf{s}) = \sum_{j=1}^{3} d_j\phi_j(\mathbf{s}) + \sum_{i=1}^{n} c_i\psi_i(\mathbf{s}) = d_1 + d_2 x + d_3 y + \sum_{i=1}^{n} c_i\psi_i(\mathbf{s}),$$

where $\phi_j(\mathbf{s})$ are polynomials of degree 1, such that $\phi_1(\mathbf{s}) = 1$, $\phi_2(\mathbf{s}) = x$ and $\phi_3(\mathbf{s}) = y$, and the Green function $\psi_i(\mathbf{s})$ is defined as $E_i(\mathbf{s}_i, \mathbf{s}) = E_i(||\mathbf{s}_i - \mathbf{s}||) =$

$|\mathbf{s}_i - \mathbf{s}|^2 \log ||\mathbf{s}_i - \mathbf{s}||$. The coefficients c_i are restricted to satisfy the boundary conditions $\sum_{i=1}^{n} c_i \phi_j(\mathbf{s}) = 0$ for $j = 1, \ldots, 3$ to make model (6) identifiable. Therefore, the spline is obtained as a weighted average of the observed data because the optimal estimate of $f(\mathbf{x}_s, \mathbf{y}_s)$ turns out to be linear in observations. When using the Green function as generalized covariance function, Tps is equivalent to kriging (Matheron, 1981; Stein, 1991), capturing the geostatistical dependence between spatial data. The command `Tps` of the *fields* `R` package (Nychka et al., 2015) estimates second-order thin-plate spline models by fitting a surface to irregularly spaced data. The smoothing parameter is chosen by generalized cross-validation or by restricted maximum likelihood.

3 MODIS data

In this study, NDVI and LST multi-temporal remote-sensing data are downloaded from the TERRA and AQUA satellites of the Moderate Resolution Imaging Spectroradiometer (MODIS, 2017), and later cropped to the border of the Spanish region of Navarre, located in the northcentral Iberian Peninsula. NDVI is a very popular index for monitoring the vegetation growth, and it is widely used in many agricultural and environmental applications (e.g. Slayback et al., 2003; Tucker et al., 2005). For calculating NDVI, we need the radiometric information obtained for the red (R) and near-infrared (NIR) wavelengths of the electromagnetic spectrum. Then, $NDVI = ((NIR) - R)/((NIR) + R)$ (Rouse Jr et al., 1974). This is a very sensitive index that takes values between 0 and 1 (van Wijk and Williams, 2005), but raw MODIS NDVI are between 0 and 10000. It is widely accepted that small values of NDVI correspond to water or snow, NDVI values between 0.2 to 0.5 can indicate bare soils and sparse vegetation, values between 0.5 and 0.7 belong to middle vegetation, and values between 0.7 and 1 indicate dense vegetation such as forests or crops at their peak growth stage.

MODIS (TERRA and AQUA) provides the red (R) and near-infrared (NIR) wavelengths to define a daily NDVI image and also the 16-day composite NDVI images. In the simulation study, we retrieve composite images from 2003 to 2016. To achieve an even number of images every year, we download 23 available composite images from Version 5-MYD13A2 (AQUA) and an additional image of November from Version-5 MOD13A2 (TERRA). This step is not a constraint in the procedure, but it helps to balance the yearly decomposing process because we use the same number of images for every time period.

Land surface temperature (LST) is an important variable that combines the results of the interaction between the atmosphere and the ground. For deriving the raw LST images from MODIS, the thermal infrared (TIR) band channels, 31 (10.78-11.28 μm) and 32 (11.77-12.27 μm), are required (Benali et al., 2012), where the split-window algorithm (Wan and Dozier, 1996; Wan et al., 2002) is a common procedure for correcting the atmospheric effects and the emissivity effects. This algorithm also uses the MODIS Land Cover product (MOD12C1). The 8-day composite images of LST day correspond to the eight-day average LSTs of the Version-5 MOD11A1 product. This compositing period is chosen because the exact ground track repeat period of the TERRA platform is 16 days.

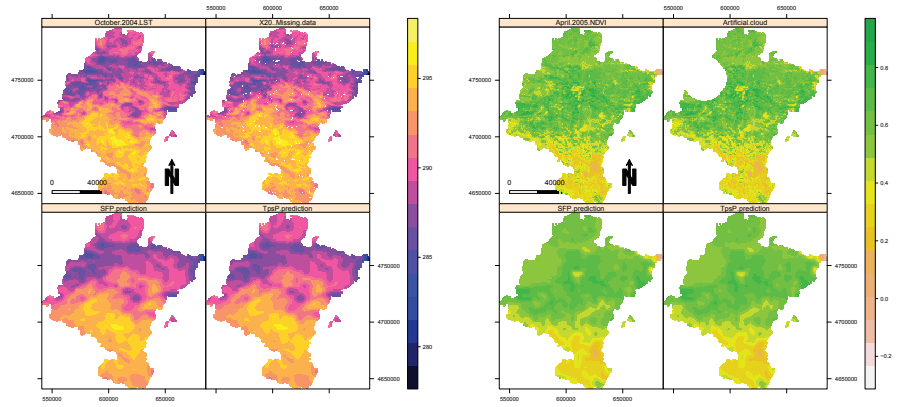

Fig. 3 On the left and from the top to the bottom, the 4 panels correspond to the LST day composite image of October_2004, the distorted image with a 20% of missing data, and the predicted images by SFP and TpsP, respectively. On the right and from the top to the bottom, the 4 panels correspond to the NDVI composite image of April_2005, the image with a 20 km radius of artificial cloud, and the predicted images by SFP and TpsP, respectively.

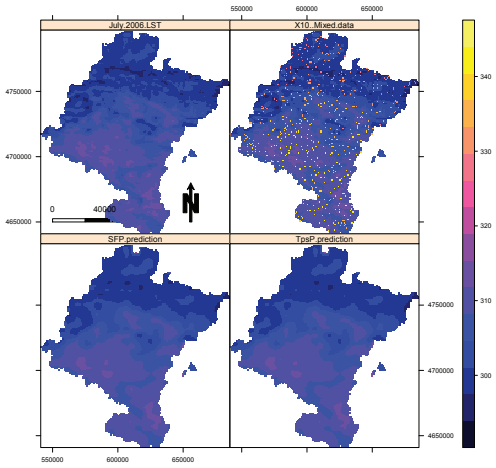

Fig. 4 From the left upper panel, the LST day composite image of July_2006 and the distorted image with a 10% mixture of missing and altered data in equal proportions. At the bottom of the figure, the predicted images by SFP and TpsP.

Each NDVI or LST day image has been imported in *R* software in rasters of dimension 166×154 with a resolution of 940.6629×940.5627 square metres, where 11741 pixels are inside the Navarre borders.

Table 1 Column 1 specifies the four scenarios of the simulation study: a) with missing data, b) with altered data and different percentages of distortion, c) with mixtures of missing and altered data, and d) with different clouds of missing data. Column 2 presents the aggregation factor (Agg. factor), except for scenario b) that gives the percentage of distortion. Columns 3-6 present the root mean square error (RMSE) in the Navarre region and in the specific target dataset of the 144 LST images from 2004 and 2015, predicted with SFP and TpsP. Columns 7 and 8 present the running time (in minutes) of the procedures.

a) Missing data	Agg. factor	Navarre RMSE SFP	Navarre RMSE TpsP	Target set RMSE SFP	Target set RMSE TpsP	Running time SFP	Running time TpsP
5%	4	0.62	0.64	0.66	0.67	1.60	4.13
10%	4	0.63	0.64	0.66	0.68	1.72	4.09
20%	4	0.63	0.65	0.67	0.69	1.64	4.11
5%	3	0.48	0.50	0.57	0.59	6.80	16.68
5%	2	0.33	0.33	0.57	0.57	12.93	1h.30
b) Altered data	Distortion percentage	Navarre RMSE SFP	Navarre RMSE TpsP	Target set RMSE SFP	Target set RMSE TpsP	Running time SFP	Running time TpsP
5%	5%	0.64	0.65	0.76	0.77	2.93	5.66
5%	10%	0.69	0.70	0.98	0.99	2.17	5.39
5%	20%	0.83	0.84	1.61	1.62	1.44	5.57
10%	5%	0.68	0.69	0.83	0.84	2.04	5.39
10%	10%	0.80	0.81	1.17	1.18	1.40	5.43
10%	20%	1.14	1.14	2.00	2.00	1.53	5.42
20%	5%	1.01	1.01	1.33	1.33	1.41	5.40
20%	10%	1.60	1.60	2.33	2.32	1.43	5.40
20%	20%	2.86	2.86	4.30	4.31	1.26	5.42
c) Miss/altered data	Agg. factor	Navarre RMSE SFP	Navarre RMSE TpsP	Target set RMSE SFP	Target set RMSE TpsP	Running time SFP	Running time TpsP
5%	4	0.65	0.66	0.74	0.75	2.06	5.39
10%	4	0.69	0.70	0.88	0.89	2.23	5.86
20%	4	0.78	0.78	1.02	1.02	1.54	5.34
d) Cloud radius	Agg. factor	Navarre RMSE SFP	Navarre RMSE TpsP	Target set RMSE SFP	Target set RMSE TpsP	Running time SFP	Running time TpsP
10 km	4	0.81	0.82	3.17	3.19	1.87	4.36
15 km	4	1.02	1.03	3.49	3.51	1.76	4.32
20 km	4	1.28	1.29	3.60	3.63	1.68	4.30

4 Simulation Study

The simulation study involves $644 = 46 \times 14$ composite images of LST day and $336 = 24 \times 14$ composite images of NDVI from 2003 to 2016. Both time series have been monthly averaged for clarifying and simplifying the decomposing process, providing two time series of $168 = 12 \times 14$ images, yet this step is not necessary for using the SFP procedure.

The simulation study consists of four different scenarios. These scenarios are defined for every image of the LST day and NDVI time series. In scenario a), we randomly introduce $5, 10$, and 20% of missing data. In scenario b), we randomly choose three sets of $5, 10$, and 20% of remote-sensing data. In every set, we modify the remote-sensing data altering three times the original data by altering $5, 10$, and 20% the original values. For example, altering 5% of the 20000 pixels of an image means that we modify the original values of 10000 pixels with three different

quantities: first, with a 5%, second with a 10%, and third, with a 20 %. In scenario c), we generate three mixtures of 5, 10 and 20% of both missing data and altered data. In this case, the remote-sensing data are modified with a 5% of distortion. In scenario d), we include artificial clouds of radius 10, 15, and 20 km.

Hence, the SFP and TpsP procedures are as follows. 1) We reduce the number of missing data and outliers in the altered input images by averaging the remote-sensing data in windows of 4×4 pixels. The window size can be changed according to the image resolution. When the aggregation factor is 4, 3 or 2, each input image has 818, 1413, or 3056 pixels, respectively. 2) We additively decompose the averaged time series of the images into a trend, a seasonal, and an error component. The decomposition process implies losing the first 6 and last 6 images of every time series. To have complete years, we have discarded the first 12 and last 12 months of both time series. Now, input time series have 144 periods corresponding to 12 months from 2004 to 2015.

3) When using SFP, we define the spatial functional data, and we predict the trend component using the ordinary kriging procedure okfd from the geofd R package (Giraldo et al., 2012). We fit different covariances of the Matérn family where the estimated ranges vary between 70 and 80 km. When using TpsP, we predict the trend component using the Tps command from the fields R package (Nychka et al., 2015).

4) We add back the seasonal and error component to both predictions in the original image resolution.

From the top left corner to the bottom right of Figure 3, we see the LST day composite image of October 2004, the altered image with a 20% of missing data, and the smoothed images by SFP and TpsP, respectively, and on the right, we see the NDVI composite image of April 2005, the same image with a random artificial cloud of 20 km radius, and the smoothed images by SFP and TpsP, respectively. In both simulated scenarios, SFP and TpsP show a similar performance, retrieving the original pattern of the remote-sensing data.

Figure 4 shows the LST day image of July 2006 (at the top left corner) and the altered image with a mixture of 10% missing data and outliers (at the top right). At the bottom, the SFP and TpsP predictions are shown. Note that the altered image has a maximum value equal to 340 Kelvin degrees, while the raw data have a maximum equal to 315 Kelvin degrees; however, the SFP and TpsP predictions retrieve the pattern of the original data and reduce the impact of altered data to a maximum of 320 Kelvin degrees.

Column 1 of both Tables 1 and 2 show the four scenarios of the simulation study. Column 2 shows the aggregation factor (Agg. factor), except for scenario b) that shows the percentage of distortion. The aggregation factor of this scenario is equal to 4. Columns 3-6 of Table 1 show the RMSE of the LST day remote-sensing data, calculated with SFP and TpsP in both domains: the Navarre region and in the target dataset. The same columns in Table 2 show the corresponding RMSE estimate of the NDVI remote-sensing data.

The main conclusion for Table 1 is that in all the scenarios, the RMSE estimated with SFP is equal or smaller than the RMSE estimated with TpsP and that SFP is faster than TpsP. Additionally, we can observe, as expected, that in all the scenarios, the RMSE calculated in the target dataset is higher than in the Navarre region, and the highest RMSE values correspond to scenario d), filling clouds. Overall, the RMSE values are very similar in scenarios a) and c), though

Table 2 Column 1 specifies the following four scenarios of the simulation study: a) with missing data, b) with altered data and different percentages of distortion, c) with mixtures of missing and altered data, and d) with different clouds of missing data. Column 2 shows the aggregation factor (Agg. factor), except for scenario b) that gives the percentage of distortion. Columns 3-6 present the root mean square error (RMSE) in the Navarre region and in the specific target dataset of the 144 NDVI images from 2004 and 2015, predicted with SFP and TpsP. Columns 7 and 8 present the running time (in minutes) of the procedures.

a) Missing data	Agg. factor	Navarre RMSE		Target set RMSE		Running time	
		SFP	TpsP	SFP	TpsP	SFP	TpsP
5%	4	0.0689	0.0702	0.0712	0.0713	2.86	5.94
10%	4	0.0689	0.0703	0.0711	0.0717	2.21	6.03
20%	4	0.0691	0.0705	0.0715	0.0717	2.29	6.01
5%	3	0.0608	0.0621	0.0654	0.0666	5.21	19.1
5%	2	0.0489	0.0494	0.0581	0.0587	19.62	2h
b) Altered data	Distortion percentage	Navarre RMSE		Target set RMSE		Running time	
		SFP	TpsP	SFP	TpsP	SFP	TpsP
5%	5%	0.0688	0.0690	0.0684	0.0686	2.41	6.17
5%	10%	0.0688	0.0690	0.0685	0.0686	2.32	6.24
5%	20%	0.0690	0.0692	0.0687	0.0690	2.40	6.35
10%	5%	0.0688	0.0690	0.0687	0.0690	2.36	6.39
10%	10%	0.0690	0.0692	0.0685	0.0688	2.66	6.42
10%	10%	0.0697	0.0699	0.0697	0.0699	2.87	6.08
20%	5%	0.0689	0.0691	0.0685	0.0688	2.55	6.00
20%	10%	0.0696	0.0697	0.0692	0.0694	2.25	5.95
20%	20%	0.0723	0.0724	0.0726	0.0728	2.30	5.96
c) Miss/altered data	Agg. factor	Navarra RMSE		Target set RMSE		Running time	
		SFP	TpsP	SFP	TpsP	SFP	TpsP
5	4	0.0697	0.0702	0.0708	0.0714	2.4	5.70
10	4	0.0698	0.0703	0.0712	0.0717	2.2	5.515
20	4	0.0699	0.0704	0.0712	0.0717	2.2	5.61
d) Cloud radius	Agg. factor	Navarre RMSE		Target set RMSE		Running time	
		SFP	TpsP	SFP	TpsP	SFP	TpsP
10 km	4	0.0738	0.0742	0.1749	0.1760	1.77	4.18
15 km	4	0.0802	0.0806	0.1896	0.1906	1.86	5.19
20 km	4	0.0894	0.0896	0.1928	0.1940	1.96	4.16

both increase noticeably when increasing the altering percentage of the distortion. Finally, in scenario a), RMSE is not sensible to a small or moderate number of missing data, but the aggregation factor significantly increases the computational cost in TpsP.

We can also draw the same conclusions for Table 2 in all the scenarios, except for scenario b), where RMSE estimated with SFP is also lower than TpsP RMSE, but both are slightly higher in the Navarre region than in the target dataset. However, running time shows large differences between both methods and undoubtedly in favour of SFP.

The standard errors of the trend predictions are calculated in all methods, and no other source of variability is considered because the decomposition of the time series is usually seen as a deterministic step. In all scenarios and variables a great computational cost is observed for TpsP. SFP and TpsP have different estimation techniques; therefore, facing and interpreting jointly both results is not a simple

task. When the aggregation factor is equal to 4, SFP provides on average a prediction standard error of 5.5 Kelvin degree in scenarios a), b) and c) and between 8 and 12 Kelvin degrees in scenario d). TpsP provides an average prediction standard error of 0.45 Kelvin degrees in the first three scenarios and 2 Kelvin degrees in scenario d). When reducing the aggregation factor to 3 or 2, the prediction standard errors reduce to 4 and 3 degrees in SFP and 0.35 and 0.3 degrees in TpsP, respectively. In scenarios a), b) and c), the SFP method applied to NDVI gives on average a prediction standard error equal to 0.08 with a factor equal to 4, 0.04 with a factor equal to 3, and 0.01 with a factor equal to 2. TpsP provides a prediction standard error estimate approximately equal to 0.03 in all cases. Therefore, TpsP provides similar prediction standard error estimates in all the scenarios, lower than SFP but with a great computer cost, while the running time for SFP is negligible.

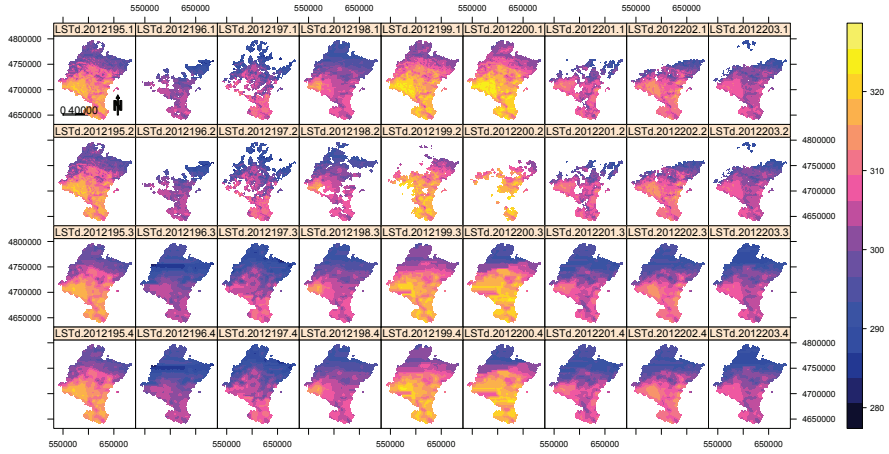

Fig. 5 Land surface temperature (LST) daily day images of Navarre between the 13th and 21st July 2012, consecutively named from LSTd_2012195.1 to LSTd_20122013.1. The first row corresponds to the input time series of images. In the second row, central images LSTd_2012198.2, LSTd_2012199.2, and LST2_2012200.2 are masked with real clouds. The third and fourth rows, with suffixes equal to 3 and 4 correspond to the predicted images with SFP and TpsP, respectively.

5 Gap-filling of daily remote-sensing data

The SFP procedure is also illustrated for filling a real target dataset of 3 LST day and 3 NDVI remote-sensing data of Navarre, corresponding to the 16th, 17th and 18th July 2012, named (LSTd/NDVI)_2012198.1, (LSTd/NDVI)_2012199.1, and (LSTd/NDVI)_2012200.1, respectively. In the first step, we aggregate the remote-sensing data in every image, calculating the means over a 4×4 and a 5×5 pixel window. For the decomposing process, a neighbour of images from the same, previous and subsequent years is required. In this example, the neighbour is defined with 27 (9 every year) daily images of LST day and 27 daily images of NDVI,

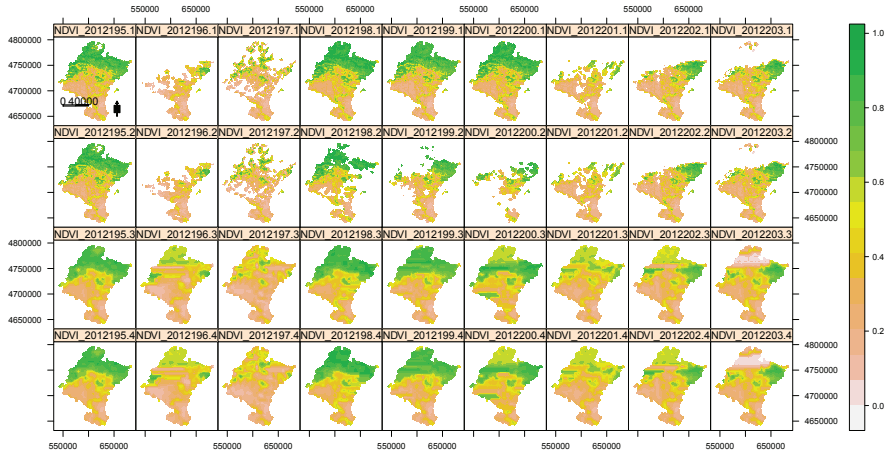

Fig. 6 Normalized difference vegetation index (NDVI) daily images of Navarre between the 13th and 21st July 2012, named consecutively from NDVI_2012195.1 to NDVI_20122013.1. The first row corresponds to the input image time series. In the second row, central images NDVI_2012198.2, NDVI_2012199.2, and NDVI_2012200.2 are masked with real clouds. The third and fourth rows, with suffixes equal to 3 and 4 correspond to the predicted images with SFP and TpsP, respectively.

downloaded from MODIS between the 13th to 21st July 2011, 2012 and 2013. In the upper panel of Figure 5, we see the observed daily images of LST day, consecutively named LST_2012194.1 to LST_2012203.1. The second panel of the same figure shows the input time series of LST day images where the 3 central target images, ((LST/NDVI)_2012198.2, (LST/NDVI)_2012199.2 and (LST/NDVI)_2012200.2 of 2012), originally without clouds, have been masked with real clouds of the 3rd, 14th and 21st July 2011. The third and fourth rows, with suffixes equal to 3 and 4 correspond to the predicted images with SFP and TpsP, respectively. Figure 6 shows the same neighbourhood and masking process, but for NDVI. Both SFP and TpsP filling procedures are applied to the trend component of the data, and the final predictions are obtained summing the predicted trend to the seasonal and error component. The comparison is made with the root mean square error (RMSE) in the 3 central images of 2012, where we know the real data.

Table 3 shows the remote-sensing data, the aggregation factor, the RMSE estimated with SFP and TpsP, and the running time of both methods. The RMSE is calculated in both the Navarra region and the specific target dataset in the three masked images LST/NDVI_2012198.2, LST/NDVI_2012199.2 and LST/NDVI_2012200.2 of 16th, 17th and 18th July 2012. In both variables, the RMSE calculated by TpsP is approximately 2.5% higher than the RMSE of SFP in Navarre and in the clouds with the aggregation factor of 4, and 2% higher when the aggregation factor is 5.

Table 3 Remote-sensing data, aggregation factor, root mean square error (RMSE) estimated with SFP and TpsP, and the running time (in minutes) of both methods. The RMSE is calculated in the Navarra region and in the specific target dataset of real clouds for the LST/NDVI_2012198, LST/NDVI_2012199 and LST/NDVI_2012200 masked images of 16th, 17th and 18th July 2012.

Remote-sensing data	Agg. factor	Navarre RMSE SFP	Navarre RMSE TpsP	Target set RMSE SFP	Target set RMSE TpsP	Running time SFP	Running time TpsP
LST day	4	3.4483	3.5158	4.3049	4.3632	1.35	7.91
NDVI	4	0.1235	0.1263	0.1526	0.1561	0.19	6.38
LST day	5	3.2982	3.3698	4.0422	4.1084	0.54	2.21
NDVI	5	0.1184	0.1202	0.1409	0.1430	0.39	2.26

Conclusions

Filling missing data or smoothing outliers in satellite imagery is a necessary task when monitoring the time series of remote-sensing data. The literature is prolific in this area because it is a relevant subject where many mathematical methods based on harmonic analysis, wavelet transform, logistic models, fusion of images or filtering techniques have been developed. However, the use of geostatistical methods, where spatial dependence is taken into account is still scarce. In this paper, we propose a new procedure called SFP that accommodates spatial dependence in functional data. The functional data are defined as the time series of remote-sensing data in each pixel of a given image. SFP is fitted with the geofd package of R that uses an ordinary kriging on the spatial functional data to provide predictions in all the pixels of every image, with missing values or not. The procedure is easily accessible, very fast, and provides accurate predictions even for long time series of images. The proposes method is compared with another procedure based on thin-plate splines (TpsP) through the RMSE. The alternative method is chosen because it also accommodates spatial dependence within remote-sensing data, and it can be applied to the trend component of the input time series of images in a similar way as SFP. In all the scenarios of the simulation study, an RMSE reduction of 1% is obtained when using the SFP method for NDVI, and a 2% RMSE reduction is obtained when using SFP for LST day. However, when using real data, we can reach a reduction of 2.5% in both sets of remote-sensing data. Additionally, SFP jointly processes all the time series of images in space and time, while TpsP needs to be run separately for every image. Consequently, in terms of computational time, the new procedure is faster, a crucial feature when analysing an increasing number of images as it could be the case in many real applications.

Acknowledgements This research was supported by Project MTM2017-82553-R (AEI/FEDER, UE), and by la Caixa Foundation (ID 1000010434), Caja Navarra Foundation, and UNED Pamplona, under agreement LCF/PR/PR15/51100007.

References

Addink, E. (1999). A comparison of conventional and geostatistical methods to replace clouded pixels in NOAA-AVHRR images. *International Journal of Remote*

Sensing, 20(5):961–977.

Aguilera-Morillo, M., Durbán, M., and Aguilera, A. (2017). Prediction of functional data with spatial dependence: a penalized approach. *Stoch. Environ Res Risk Assess*, 31(1):7–22.

Benali, A., Carvalho, A., Nunes, J., Carvalhais, N., and Santos, A. (2012). Estimating air surface temperature in Portugal using MODIS LST data. *Remote Sensing of Environment*, 124:108–121.

Bernardi, M. S., Sangalli, L. M., Mazza, G., and Ramsay, J. O. (2017). A penalized regression model for spatial functional data with application to the analysis of the production of waste in Venice province. *Stochastic Environmental Research and Risk Assessment*, 31(1):23–38.

Bhavya, V. and Jaleel, S. (2014). Cloud Removal From Multi-temporal Satellite Images Using Information Cloning and Information Reconstruction. *International Journal of Emerging Trends in Science and Technology*, 1(04).

Boer, E. P., de Beurs, K. M., and Hartkamp, A. D. (2001). Kriging and thin plate splines for mapping climate variables. *International Journal of Applied Earth Observation and Geoinformation*, 3(2):146–154.

Brooks, E., Wynne, R., and Thomas, V. (2018). Using window regression to gap-fill landsat etm+ post slc-off data. *Remote Sensing*, 10(10):1502.

Cai, Z., Jönsson, P., Jin, H., and Eklundh, L. (2017). Performance of smoothing methods for reconstructing ndvi time-series and estimating vegetation phenology from modis data. *Remote Sensing*, 9(12):1271.

Cleveland, R. B., Cleveland, W. S., McRae, J. E, and Terpenning, I. (1990). STL: A seasonal-trend decomposition procedure based on loess. *Journal of Official Statistics*, 6(1):3–73.

Cressie, N. and Wikle, C. K. (2015). *Statistics for spatio-temporal data*. John Wiley & Sons.

Delicado, P., Giraldo, R., Comas, C., and Mateu, J. (2010). Statistics for spatial functional data: some recent contributions. *Environmetrics: The official journal of the International Environmetrics Society*, 21(3-4):224–239.

Durbin, J., Koopman, S. J. (2002). A simple and efficient simulation smoother for state space time series analysis. *Biometrika*, 89(3):603–616.

Eklundh, L. and Jönsson, P. (2012). TIMESAT 3.2 with parallel processing-Software Manual. *Lund University*.

Gao, Y., Xie, H., Yao, T., and Xue, C. (2010). Integrated assessment on multi-temporal and multi-sensor combinations for reducing cloud obscuration of MODIS snow cover products of the Pacific Northwest USA. *Remote Sensing of Environment*, 114(8):1662–1675.

Gerber, F., de Jong, R., Schaepman, M. E., Schaepman-Strub, G., and Reinhard, F. (2018). Predicting Missing Values in Spatio-Temporal Remote Sensing Data. *IEEE Transactions on Geoscience and Remote Sensing*, 56(5):2841–2853.

Gerber, F., Furrer, R., Schaepman-Strub, G., de Jong, R., and Schaepman, M. E. (2016). Predicting missing values in spatio-temporal satellite data. *ArXiv e-prints*.

Giraldo, R., Delicado, P., and Mateu, J. (2010). Continuous time-varying kriging for spatial prediction of functional data: An environmental application. *Journal of Agricultural, Biological, and Environmental Statistics*, 15(1):66–82.

Giraldo, R., Delicado, P., and Mateu, J. (2011). Ordinary kriging for function-valued spatial data. *Environmental and Ecological Statistics*, 18(3):411–426.

Giraldo, R., Mateu, J., and Delicado, P. (2012). geofd: an R package for function-valued geostatistical prediction. *Revista Colombiana de Estadística*, 35(3):385–407.

Goitía, A., Medina, M. R., and Angulo, J. (2005). Joint estimation of spatial deformation and blurring in environmental data. *Stochastic Environmental Research and Risk Assessment*, 19(1):1–7.

Goulard, M. and Voltz, M. (1993). Geostatistical interpolation of curves: a case study in soil science. In *Geostatistics Tróia92*, pages 805–816. Springer.

Holben, B. N. (1986). Characteristics of maximum-value composite images from temporal AVHRR data. *International Journal of Remote Sensing*, 7(11):1417–1434.

Hou, J., Huang, C., Zhang, Y., Guo, J., and Gu, J. (2019). Gap-filling of modis fractional snow cover products via non-local spatio-temporal filtering based on machine learning techniques. *Remote Sensing*, 11(1):90.

Masek, J. G., Goward, S. N., Kennedy, R. E., Cohen, W. B., Moisen, G. G., Schleeweis, K., and Huang, C. (2013). United States forest disturbance trends observed using Landsat time series. *Ecosystems*, 16(6):1087–1104.

Masek, J. G., Vermote, E. F., Saleous, N. E., Wolfe, R., Hall, F. G., Huemmrich, K. F., Gao, F., Kutler, J., and Lim, T.-K. (2006). A Landsat surface reflectance dataset for North America, 1990-2000. *IEEE Geoscience and Remote Sensing Letters*, 3(1):68–72.

Matheron, G. (1981). Splines and kriging: their formal equivalence. *Down-to-earth-statistics: Solutions looking for geological problems*, pages 77–95.

Militino, A. F., Ugarte, M. D., and Pérez-Goya, U. (2017). Stochastic Spatio-Temporal Models for Analysing NDVI Distribution of GIMMS NDVI3g Images. *Remote Sensing*, 9(1):76.

Militino, A. F., Ugarte, M. D., and Pérez-Goya, U. (2018). Improving the quality of satellite imagery based on ground-truth data from rain gauge stations. *Remote Sensing*, 10(3):398.

MODIS (2017). https://modis.gsfc.nasa.gov/about/.

Müller, H., Rufin, P., Griffiths, P., Siqueira, A. J. B., and Hostert, P. (2015). Mining dense Landsat time series for separating cropland and pasture in a heterogeneous Brazilian savanna landscape. *Remote Sensing of Environment*, 156:490–499.

Nychka, D., Furrer, R., Paige, J., and Sain, S. (2015). fields: Tools for spatial data. R package version 9.0.

Park, S.-Y., Sur, C., Kim, J.-S., and Lee, J.-H. (2018). Evaluation of multi-sensor satellite data for monitoring different drought impacts. *Stochastic Environmental Research and Risk Assessment*, pages 1–13.

Poggio, L., Gimona, A., and Brown, I. (2012). Spatio-temporal MODIS EVI gap filling under cloud cover: An example in Scotland. *ISPRS Journal of Photogrammetry and Remote Sensing*, 72:56–72.

Qiu, B., Feng, M., and Tang, Z. (2016). A simple smoother based on continuous wavelet transform: Comparative evaluation based on the fidelity, smoothness and efficiency in phenological estimation. *International journal of applied earth observation and geoinformation*, 47:91–101.

Ramsay, J. (2005). Functional data analysis. *Encyclopedia of Statistics in Behavioral Science*.

Ramsay, J. O. and Silverman, B. W. (2007). *Applied functional data analysis: methods and case studies*. Springer.

Richter, R. (1996). A spatially adaptive fast atmospheric correction algorithm. *International Journal of Remote Sensing*, 17(6):1201–1214.

Rossi, R. E., Dungan, J. L., and Beck, L. R. (1994). Kriging in the shadows: geostatistical interpolation for remote sensing. *Remote Sensing of Environment*, 49(1):32–40.

Rouse Jr, J., Haas, R., Schell, J., and Deering, D. (1974). Monitoring vegetation systems in the Great Plains with ERTS. *NASA special publication*, 351:309.

Ruiz-Medina, M. and Espejo, R. (2012). Spatial autoregressive functional plug-in prediction of ocean surface temperature. *Stochastic Environmental Research and Risk Assessment*, 26(3):335–344.

Schneider, A. (2012). Monitoring land cover change in urban and peri-urban areas using dense time stacks of Landsat satellite data and a data mining approach. *Remote Sensing of Environment*, 124:689–704.

Shen, H., Li, H., Qian, Y., Zhang, L., and Yuan, Q. (2014). An effective thin cloud removal procedure for visible remote sensing images. *ISPRS Journal of Photogrammetry and Remote Sensing*, 96:224–235.

Slayback, D. A., Pinzon, J. E., Los, S. O., and Tucker, C. J. (2003). Northern hemisphere photosynthetic trends 1982–99. *Global Change Biology*, 9(1):1–15.

Stein, M. L. (1991). A kernel approximation to the kriging predictor of a spatial process. *Annals of the Institute of Statistical Mathematics*, 43(1):61–75.

Tseng, D.-C., Tseng, H.-T., and Chien, C.-L. (2008). Automatic cloud removal from multi-temporal SPOT images. *Applied Mathematics and Computation*, 205(2):584–600.

Tucker, C. J., Pinzon, J. E., Brown, M. E., Slayback, D. A., Pak, E. W., Mahoney, R., Vermote, E. F., and El Saleous, N. (2005). An extended AVHRR 8-km NDVI dataset compatible with MODIS and SPOT vegetation NDVI data. *International Journal of Remote Sensing*, 26(20):4485–4498.

Van de Kassteele, J., Koelemeijer, R., Dekkers, A., Schaap, M., Homan, C., and Stein, A. (2006). Statistical mapping of PM10 concentrations over Western Europe using secondary information from dispersion modeling and MODIS satellite observations. *Stochastic Environmental Research and Risk Assessment*, 21(2):183–194.

van Wijk, M. T. and Williams, M. (2005). Optical instruments for measuring leaf area index in low vegetation: application in arctic ecosystems. *Ecological Applications*, 15(4):1462–1470.

Vera, J. F., Angulo, J. M., and Roldán, J. A. (2017). Stability analysis in nonstationary spatial covariance estimation. *Stochastic Environmental Research and Risk Assessment*, 31(3):815–828.

Verhoef, W., Menenti, M., and Azzali, S. (1996). Cover A colour composite of NOAA-AVHRR-NDVI based on time series analysis (1981-1992). *International Journal of Remote Sensing*, 17(2):231–235.

Wan, Z. and Dozier, J. (1996). A generalized split-window algorithm for retrieving land-surface temperature from space. *IEEE Transactions on geoscience and remote sensing*, 34(4):892–905.

Wan, Z., Zhang, Y., Zhang, Q., and Li, Z.-l. (2002). Validation of the land-surface temperature products retrieved from Terra Moderate Resolution Imaging Spectroradiometer data. *Remote sensing of Environment*, 83(1):163–180.

Wood, S. N. (2003). Thin plate regression splines. *Journal of the Royal Statistical Society: Series B (Statistical Methodology)*, 65(1):95–114.

Wood, S. N. (2017). *Generalized additive models: an introduction with R*. Chapman and Hall/CRC.

Xie, H., Wang, X., and Liang, T. (2009). Development and assessment of combined Terra and Aqua snow cover products in Colorado Plateau, USA and Northern Xinjiang, China. *Journal of Applied Remote Sensing*, 3(1):033559–033559.

Xu, H., Xu, C.-Y., Sælthun, N. R., Zhou, B., and Xu, Y. (2015). Evaluation of reanalysis and satellite-based precipitation datasets in driving hydrological models in a humid region of Southern China. *Stochastic Environmental Research and Risk Assessment*, 29(8):2003–2020.

Yang, G., Shen, H., Zhang, L., He, Z., and Li, X. (2015). A moving weighted harmonic analysis method for reconstructing high-quality SPOT VEGETATION NDVI time-series data. *IEEE Transactions on Geoscience and Remote Sensing*, 53(11):6008–6021.

Yin, G., Mariethoz, G., and McCabe, M. F. (2016). Gap-Filling of Landsat 7 Imagery Using the Direct Sampling Method. *Remote Sensing*, 9(1):12.

Zhang, C., Li, W., and Civco, D. (2014). Application of geographically weighted regression to fill gaps in SLC-off Landsat ETM+ satellite imagery. *International Journal of Remote Sensing*, 35(22):7650–7672.